Supporting information

High-Precision Assembly of Molecularly Thin Zeolite Nanosheets into Tiled Mono- and Multilayer Films for Robust Corrosion Protection

Ondřej Veselý, Nobuyuki Sakai, Yasuo Ebina, and Takayoshi Sasaki*

Research Center for Materials Nanoarchitectonics (MANA), National Institute for Materials Science (NIMS), 1-1 Namiki, Tsukuba, Ibaraki 305-0044, Japan.

*Corresponding author: SAKAI.Nobuyuki@nims.go.jp

Preparation of 2D Zeolites and the Nanosheet Suspensions

Layered zeolites MCM-56 (Figure S1a) and bifer were synthesized according to previously published protocols and their structure has been verified by powder XRD.[1,2] The diffraction pattern of the MCM-56 material exhibits a broad diffraction feature comprising of the 101 and 102 reflections (Figure S1d) characteristic for the MCM-56 and indicative of its disordered layer stacking that clearly distinguishes it from the unexfoliable MCM-22P and MCM-49 materials. The disordered nature of the MCM-56 causes significant broadening of the diffraction lines. Nevertheless, the characteristic 100, 101, 102, 220, and 310 diffraction lines are easily distinguishable and the pattern of agrees well with previously published data for the MCM-56 layered material.[3–5] The bifer zeolite comprises a mixture of two phases, a non-exfoliable ZSM-55 precursor and exfoliable bifer layers,[1] which are 1.9 nm thick. The precise structure of the bifer layers remains uncertain, with evidence suggesting possible similarities to FER and CDO framework topologies (Figure S1b, c).[6] While the exact crystal topology of the bifer layers is a matter of debate, the material can easily be identified by the characteristic 200, 031, 002, and 040 present in the XRD pattern and consistent with previously published data.[1,6,7] SEM images of MCM-56 (Figure S1e) show several micrometer-sized particles formed of small sub-micrometer sized lamellae, typical for the MCM-56 material. In contrast,

the bifer morphology resembles a series of interlocked platelet-shaped crystals from 1 to 4 μm in width (Figure S1f).

The exfoliation of MCM-56 and bifer into unilamellar nanosheets was achieved through a soft chemical route employing tetrabutylammonium hydroxide (TBAOH) solutions. The exfoliation process, involving osmotic swelling and subsequent removal of unexfoliated material by centrifugation, produced turbid suspensions containing well-dispersed nanosheets with concentrations between 0.6 and 0.8 wt%. The unexfoliated residue was subjected to a second sequence of exfoliation and centrifugation, yielding an akin suspension with concentration around 0.3 wt%. Subsequent exfoliation attempts on the residue yielded suspensions with concentrations below 0.1 wt%, rendering them impractical for further experimentation.

The MCM-56 and bifer nanosheets, which are negatively charged in their suspensions, were deposited onto flat Si substrates from appropriately diluted suspensions using several distinct methods which will be discussed individually. The AFM images generally show deposited sheets with a lateral size between 0.2 and 0.5 μm, and thickness ca. 2.5 and 2.1 nm for the MCM-56 and bifer nanosheets, respectively (Figure S2), which is consistent with previously reported data.[1,2] In-plane XRD patterns of the deposited films exhibit characteristic reflections for the MWW and FER structures (Figure S3), respectively, evidencing that the structure of the nanosheets was preserved after exfoliation and the subsequent deposition.

Influence of pH and ζ-potential on the Number of Overlaps

AFM imaging of the deposited films of MCM-56 consistently revealed minor degree of overlapping nanosheets regardless of the deposition method (Figure 1, 3, 5, Scheme S1a). Such overlaps are likely attributed to nanosheet aggregation within the suspension and are strongly dependent on the charge of the nanosheets and the ζ-potential which are affected by the pH of the suspension. Adjusting the ζ-potential through repeated sedimentation and redispersion of

nanosheets in pure water resulted in a gradual decrease in negative ζ-potential, from an initial value of −46.7 mV to −40.5 mV, −39.1 mV, and eventually −27.5 mV, accompanied by a reduction in pH towards neutrality (Figure S10g). This caused a reduction in charge, diminishing the electrostatic repulsion between nanosheets and leading to an increase in nanosheet overlaps highlighted by the growing coverage by double- or multi-layer thick film (Figure S10, S11). Conversely, higher pH promoted deprotonation of terminal silanol groups on the zeolite nanosheets, thus increasing the negative charge and improving their separation. To increase the pH value, the nanosheets were redispersed in different concentration of TBAOH, yielding ζ-potential of −45.3 mV and −33.3 mV (Figure 10g). The redispersion in 0.5% TBAOH resulted in a minor increase in overlaps between the deposited nanosheets compared to the original suspension (Figure 10e). However, upon further increasing the pH by redispersion in TBAOH, a significant aggregation of nanosheets occurred (Figure S10f, S11f). This suggests that beyond a certain limit, excessive ionic strength of the suspension outweighs the stabilizing effect of the negative charge, causing aggregation.[8,9] The suspensions obtained directly from the exfoliation without additional adjustment of the pH or washing produce the highest quality films upon deposition.

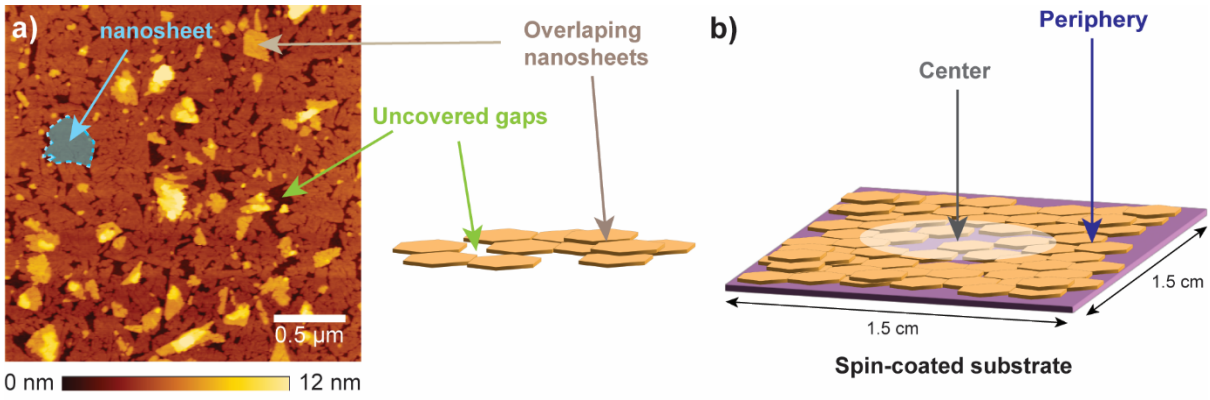

Scheme S1. (a) Example of a typical AFM image of a deposited MCM-56 nanosheets, highlighting the single-layer nanosheets, gaps, and overlaps and (b) schematic of the spin-coated substrate distinguishing the central and peripheral regions for AFM imaging.

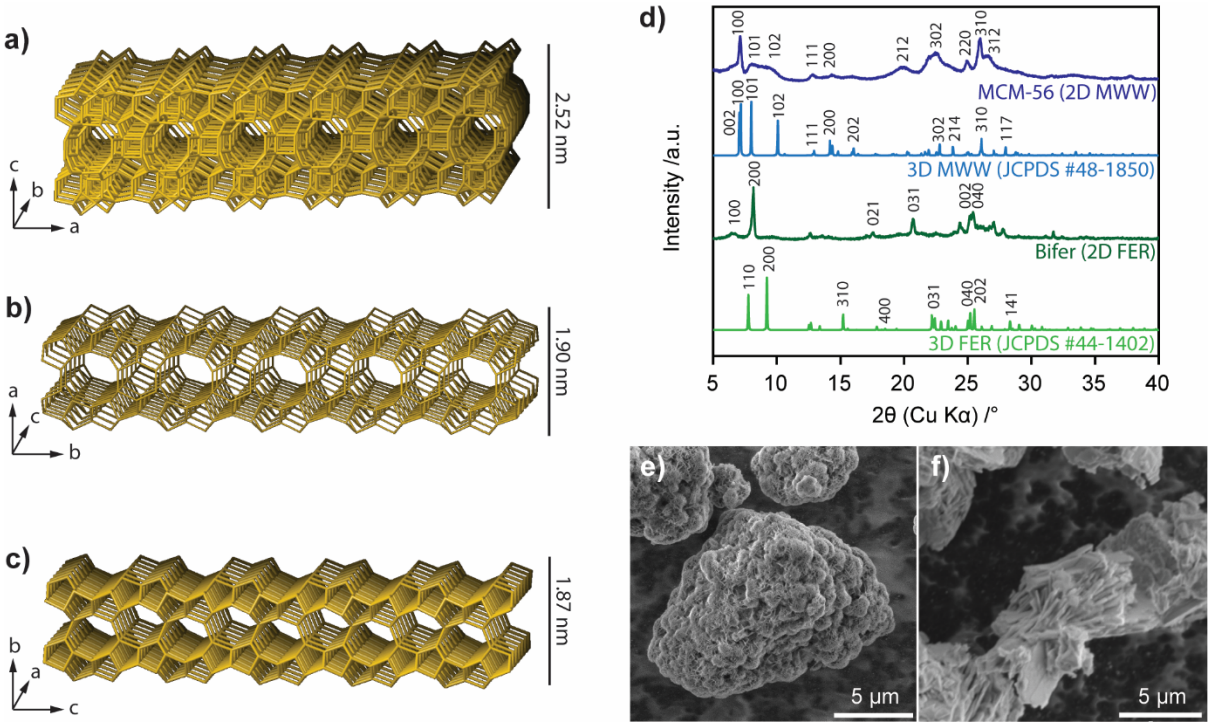

Figure S1. Structure of (a) MCM-56 layer, presumed structures of bifer layer[10]: (b) FER and (c) CDO zeolite topology, (d) powder XRD patterns of as-synthesized MCM-56 and bifer, and SEM images of (e) MCM-56 and (f) bifer samples.

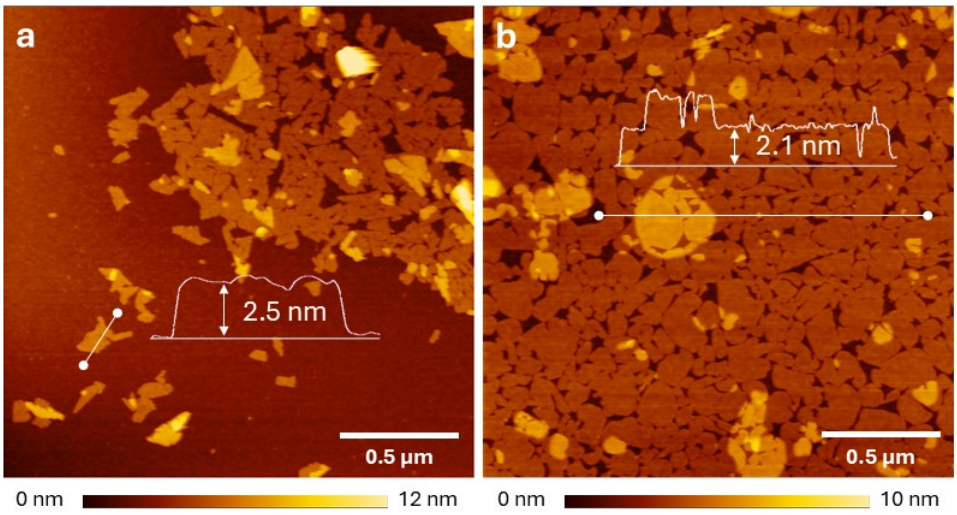

Figure S2. AFM images and height profiles of (a) MCM-56 and (b) bifer nanosheets deposited on Si wafers by spin-coating.

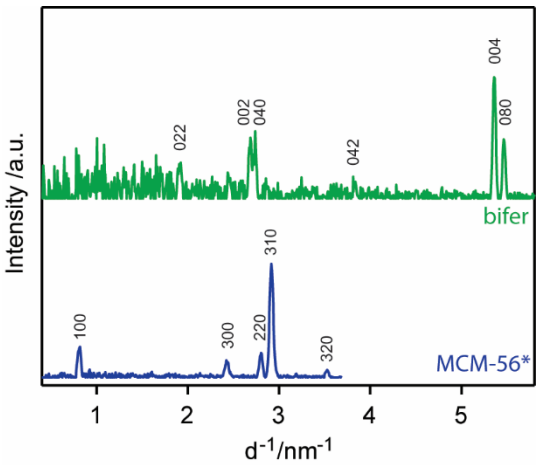

Figure S3. In-plane XRD patterns of MCM-56 and bifer nanosheet films deposited by the pick-up method (*Measurement was terminated at $d^{-1} = 3.7$ nm^{-1}).

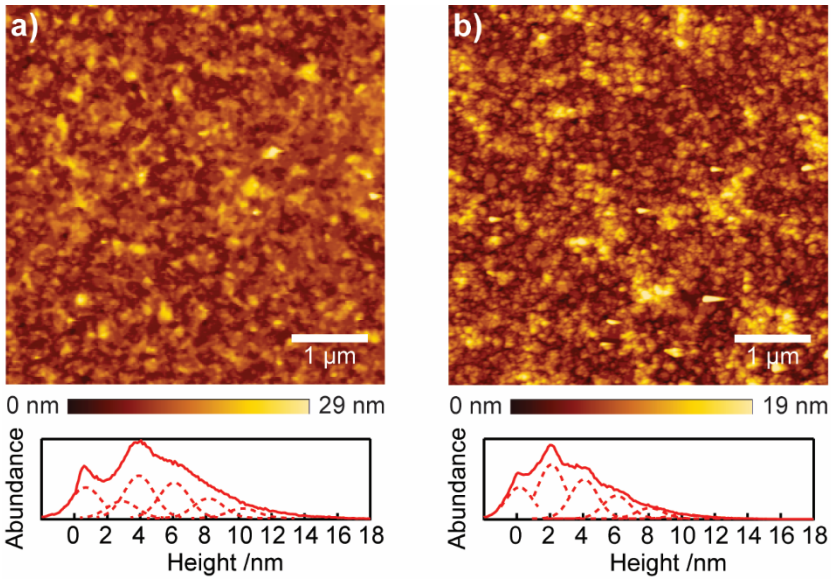

Figure S4. AFM images and corresponding height histograms of the Si wafers coated with (a) MCM-56 and (b) bifer nanosheets using the electrostatic adsorption method (15 min, 0.08 g L^{-1}, pH ≈ 9.1).

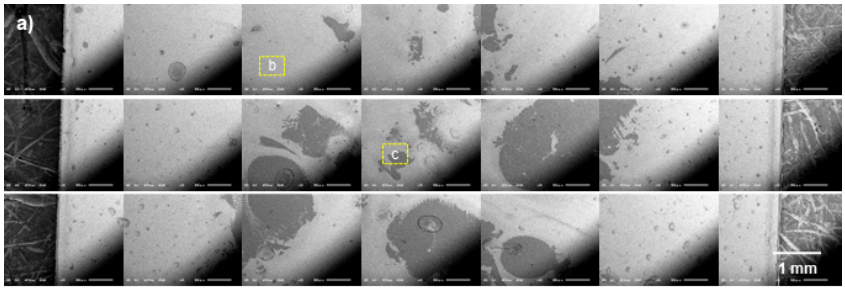
a)
b
c
1 mm

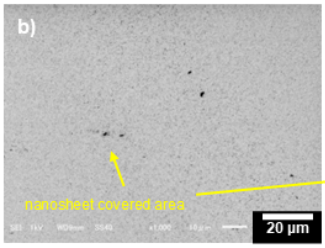
b)
nanosheet covered area
20 µm

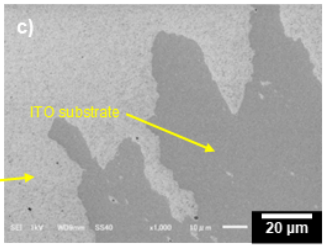
c)
ITO substrate
20 µm

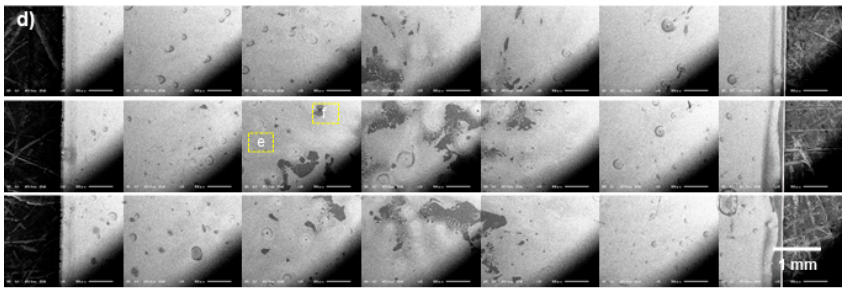
d)
e
f
1 mm

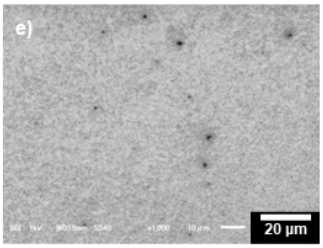
e)
20 µm

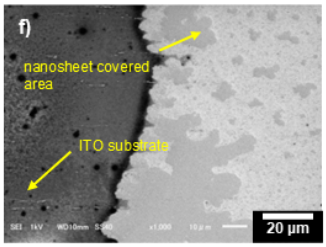
f)
nanosheet covered area
ITO substrate
20 µm

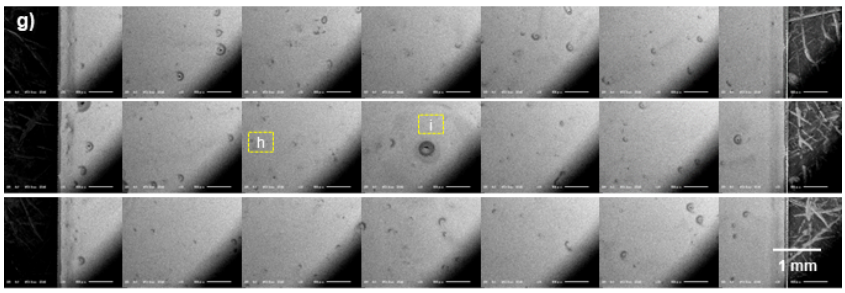
g)
h
i
1 mm

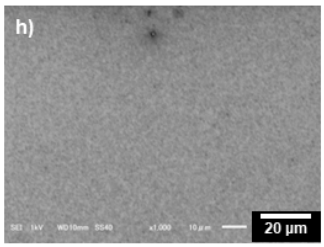
h)
20 µm

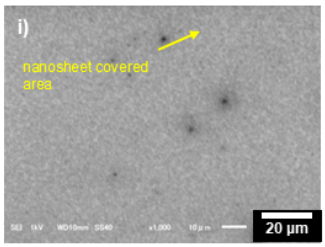
i)
nanosheet covered area
20 µm

Figure S5. Assembly of SEM images of MCM-56 nanosheets deposited on ITO substrates by spin-coating their suspension (0.4 wt% in DMSO) at (a–c) 1200, (d–f) 1100, and (g–i)1000 rpm. The locations of the magnified images (b, c, e, f, h, i) are indicated in the corresponding images (a, d, g). The size of the rectangles does not correspond to the actual size of the magnified images.

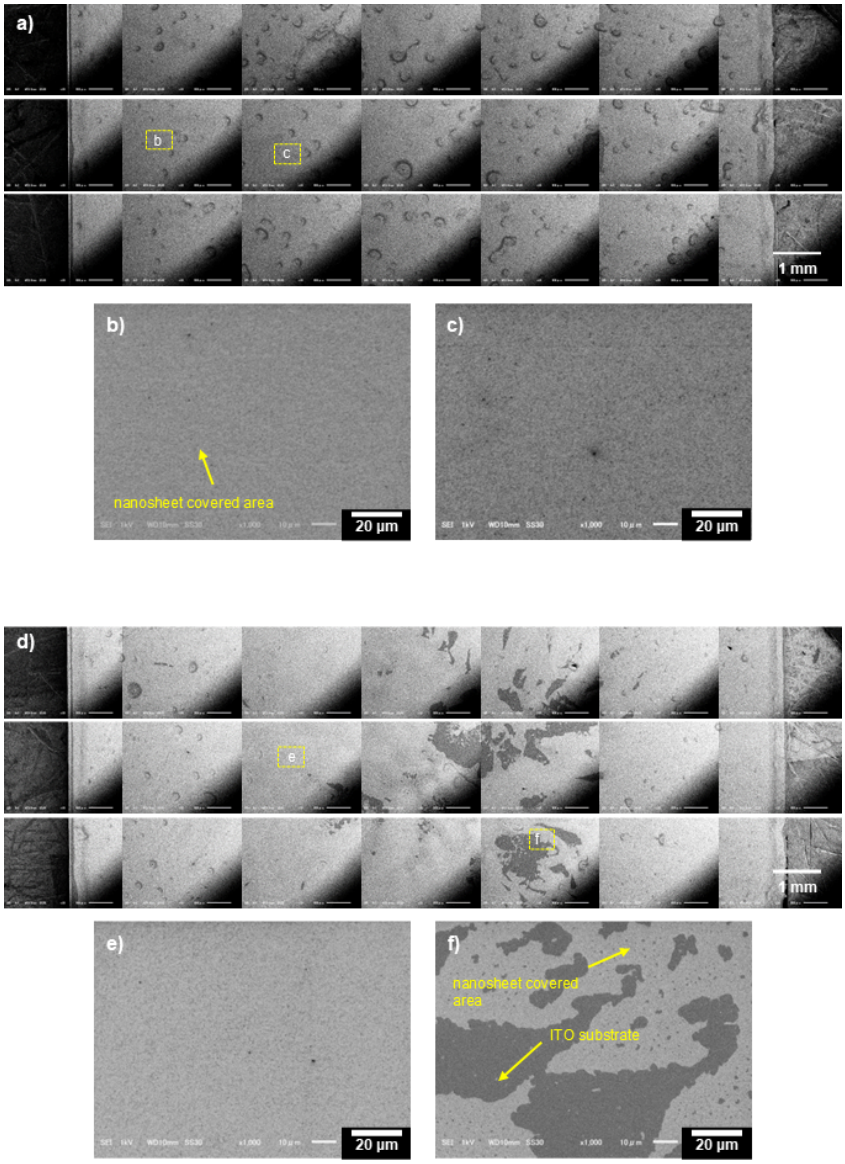

Figure S6. Assembly of SEM images of MCM-56 nanosheets deposited on ITO substrates by spin-coating their suspension (0.4 wt% in DMSO) at (a–c) 1200 rpm followed by 1000 rpm and (d–f) 1400 rpm followed by 1000 rpm. The locations of the magnified images (b, c, e, f)

are indicated in the corresponding images (a, d). The size of the rectangles does not correspond to the actual size of the magnified images.

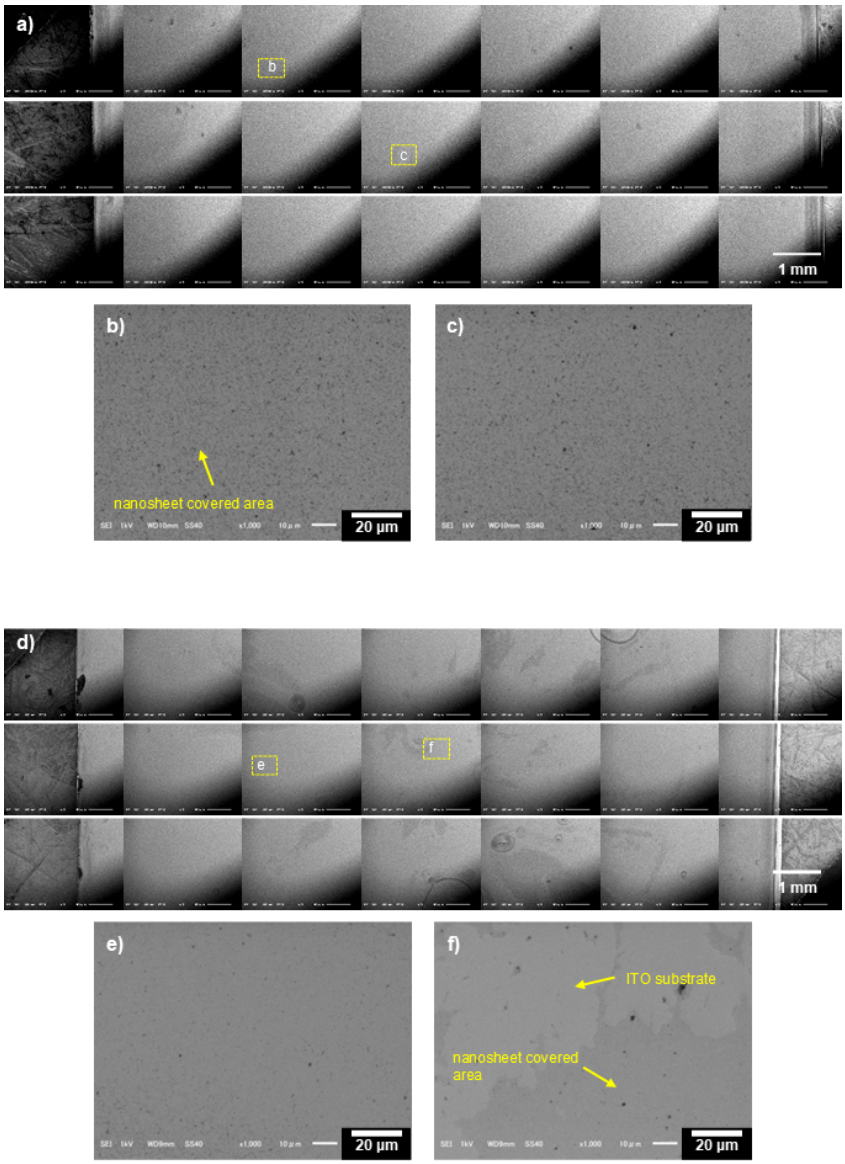

Figure S7. Assembly of SEM images of bifer nanosheets deposited by spin-coating their suspension (0.4 wt% in DMSO) at (a–c) 1000 rpm and (d–f) 1200 rpm. The locations of the magnified images (b, c, e, f) are indicated in the corresponding images (a, d). The size of the rectangles does not correspond to the actual size of the magnified images.

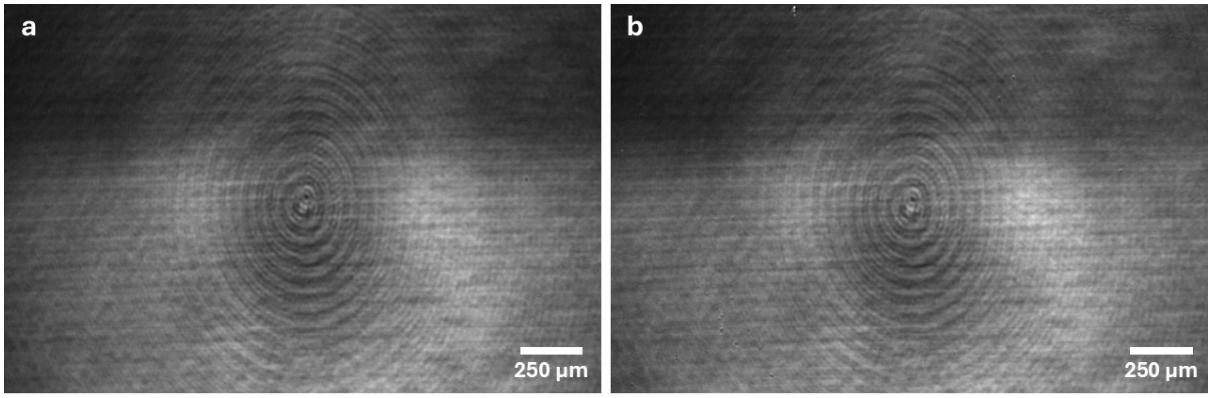

Figure S8. Brewster angle microscopy images of the film of MCM-56 on the water-air phase boundary (a) directly after deposition of the suspension with MCM-56 nanosheets; (b) after 3 min of delay.

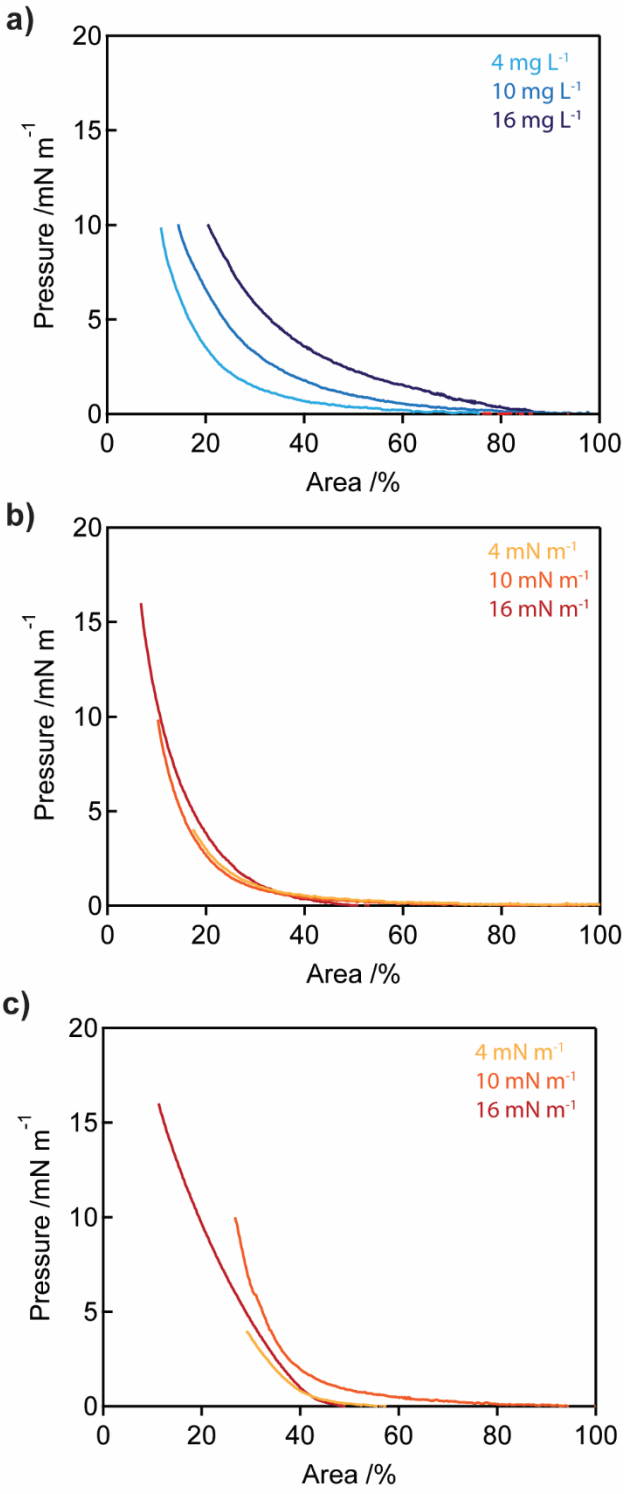

Figure S9. (a) Pressure−area (π−A) isotherms for MCM-56 nanosheet suspension at varying nanosheet concentrations; isotherms of (b) MCM-56 and (c) bifer suspensions at varying maximum surface pressures. The percentage of surface area relative to the area before compression is used for the x-axis.

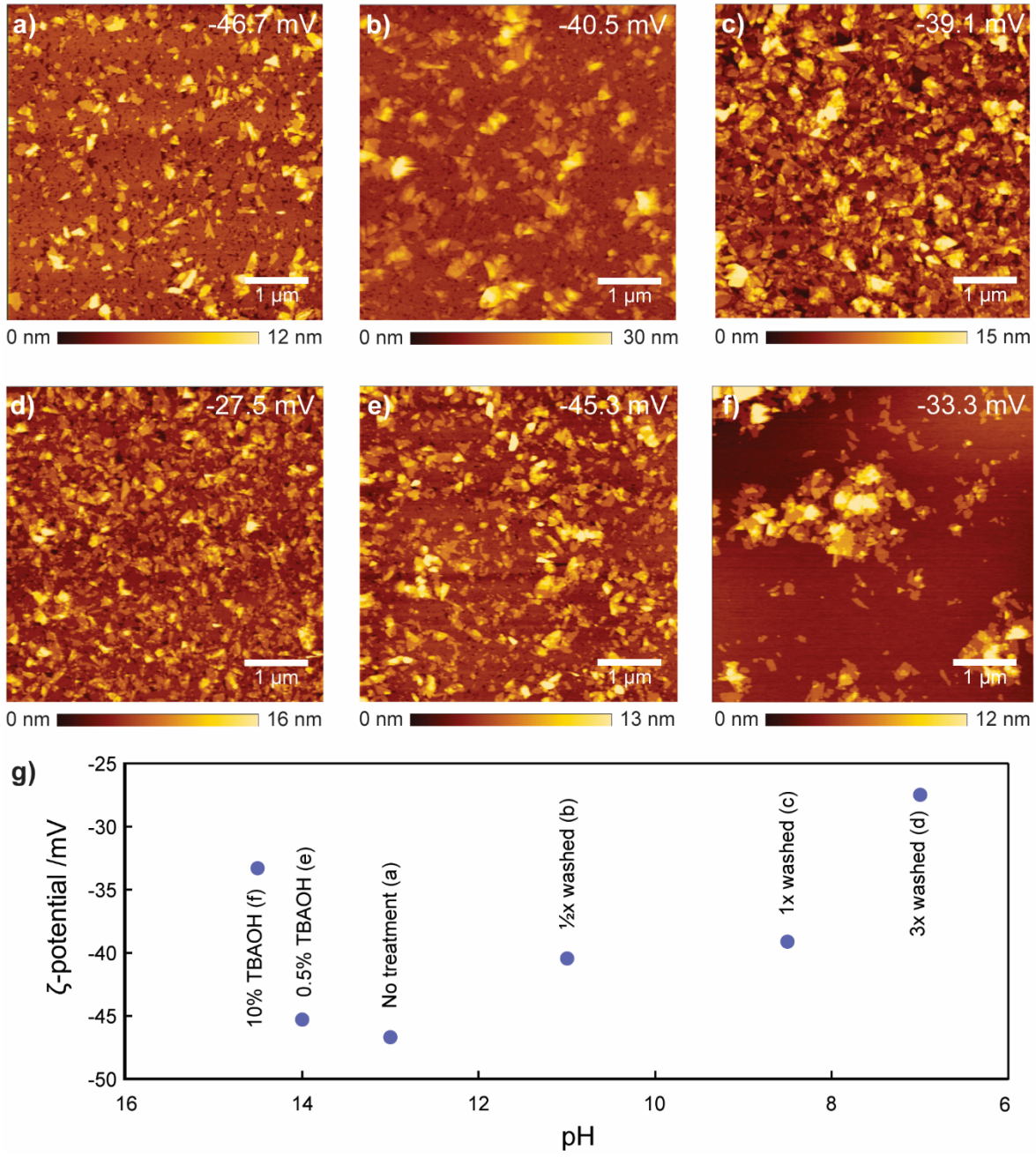

Figure S10. AFM images of the Si wafers coated using the pick-up method with suspension of (a) MCM-56 nanosheets directly after exfoliation with a ζ-potential of −46.7 mV; nanosheets redispersed in water with ζ-potentials of (b) −40.5 mV, (c) −39.1 mV, and (d) −27.5 mV; nanosheets redispersed in TBAOH with ζ-potentials of (e) −45.3 mV and (f) −33.3 mV; and (g) ζ-potentials of the individual suspensions plotted against their pH values.

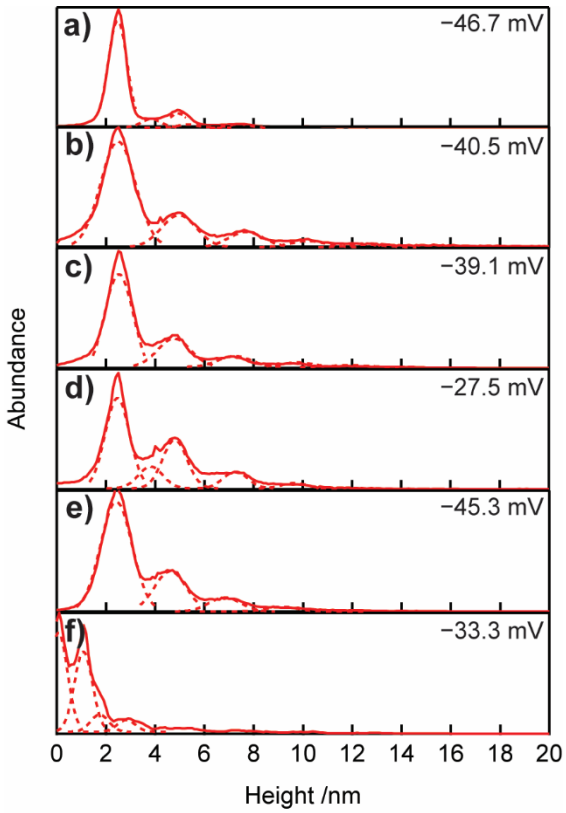

Figure S11. Height histograms of the MCM-56 films obtained from untreated suspension of MCM-56 nanosheets with ζ-potential −46.7 mV (a); nanosheets redispersed in water with −40.5 mV (b), −39.1 mV (c), −27.5 mV (d); nanosheets redispersed in TBAOH with −45.3 mV (e), −33.3 mV (f).

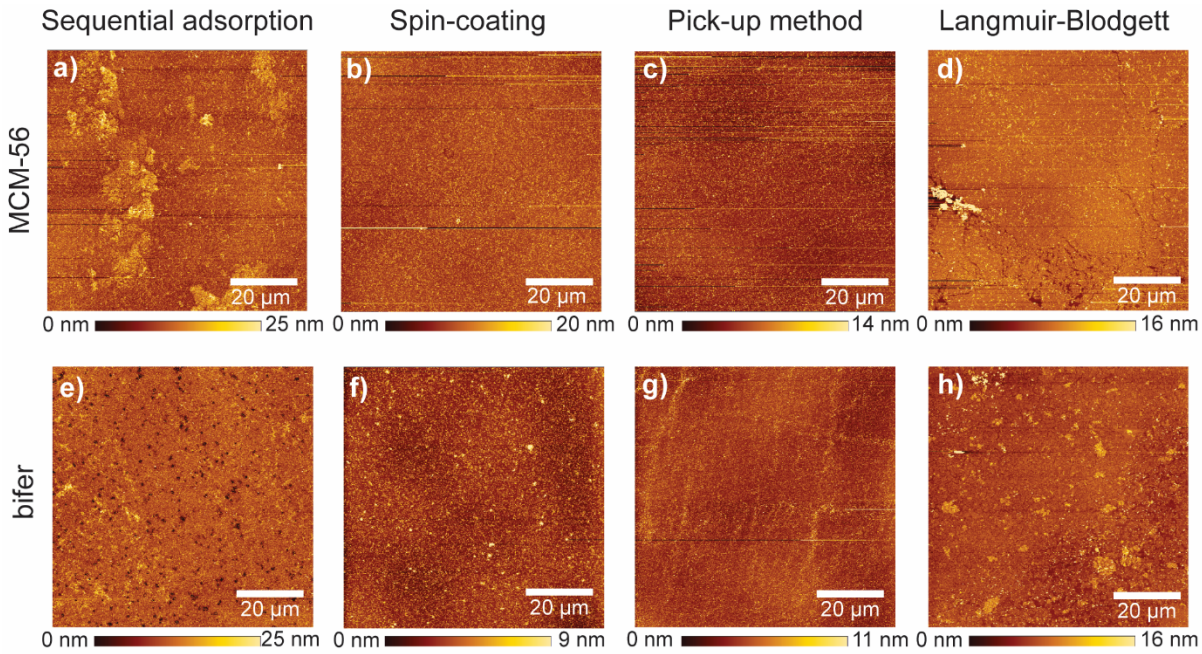

Figure S12. Large area (100 × 100 μm) AFM images of the Si wafers coated with suspension of (a-d) MCM-56 and (e-h) bifer nanosheets using the (a, e) electrostatic adsorption, (h, f) spin-coating, (c, g) pick-up and (d, h) LB method.

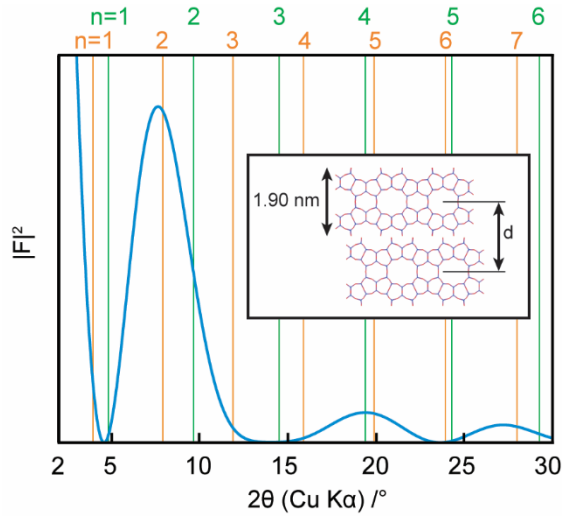

Figure S13. Square of structure factor calculated based on the bifer architecture. Orange and green lines indicate the position of the basal reflections for the intersheet spacing of 2.23 and 1.87 nm, respectively.

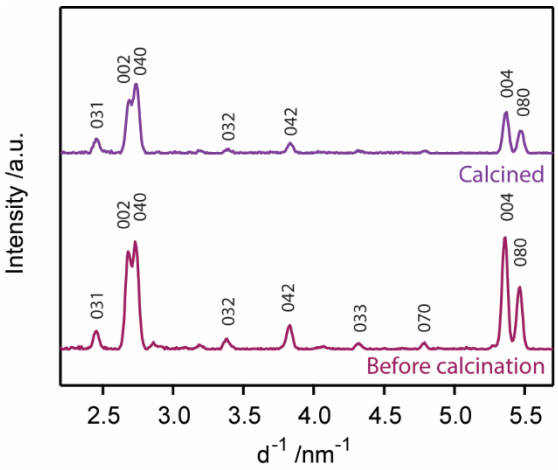

Figure S14. In-plane XRD patterns of bifer nanosheets deposited in 10 consecutive layers by the pick-up method before (purple) and after calcination (violet).

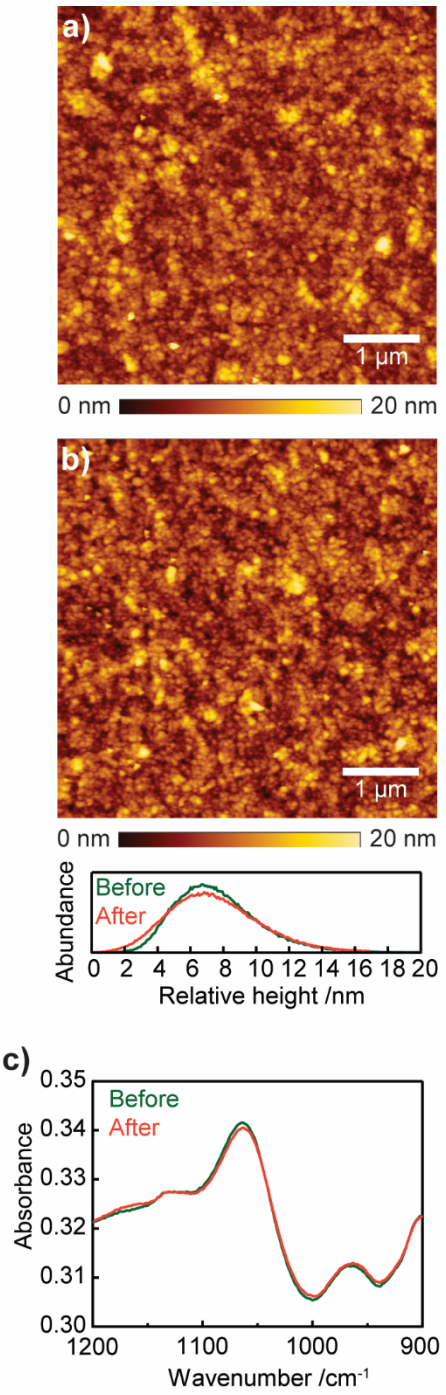

Figure S15. AFM images and corresponding height histograms of 10 layer films of bifer nanosheets deposited on the Si wafer via the pick-up method (a) before and (b) after peeling with an adhesive tape, and (c) the respective FT-IR spectra.

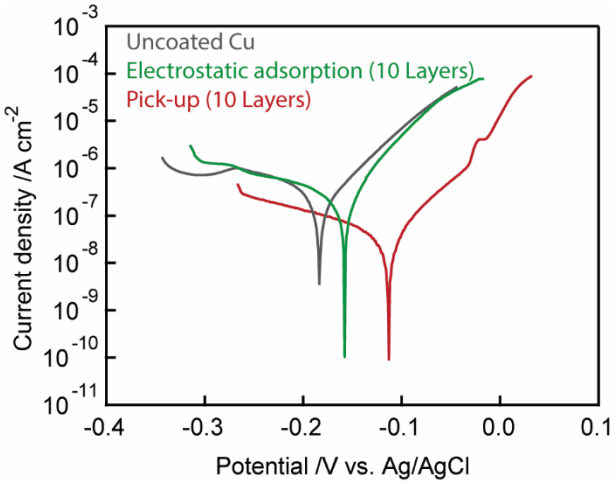

Figure S16. Potentiodynamic polarization curves of the uncoated copper plate (grey) and the copper plates coated with 10 bifer layers using the electrostatic adsorption (green) and the pick-up method (red).

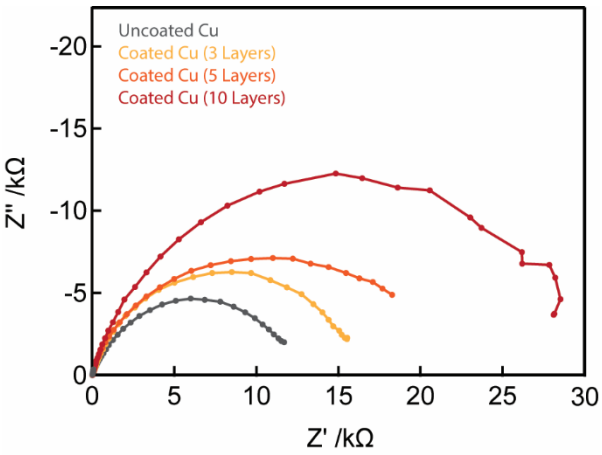

Figure S17. Electrochemical impedance spectroscopy data of the copper plates coated with 0, 3, 5, and 10 bifer layers prepared by the pick-up method.

References

(1) Wang, C.; Sakai, N.; Ebina, Y.; Kikuchi, T.; Grzybek, J.; Roth, W. J.; Gil, B.; Ma, R.; Sasaki, T. Construction of Hierarchical Films via Layer-by-Layer Assembly of Exfoliated Unilamellar Zeolite Nanosheets. *Small* **2024**, *20*, 2308293.

(2) Roth, W. J.; Sasaki, T.; Wolski, K.; Song, Y.; Tang, D.-M.; Ebina, Y.; Ma, R.; Grzybek, J.; Kałahurska, K.; Gil, B.; Mazur, M.; Zapotoczny, S.; Cejka, J. Liquid Dispersions of Zeolite Monolayers with High Catalytic Activity Prepared by Soft-Chemical Exfoliation. *Sci. Adv.* **2020**, *6*, eaay8163.

(3) Roth, W. J.; Dorset, D. L. Expanded View of Zeolite Structures and Their Variability Based on Layered Nature of 3-D Frameworks. *Micropor. Mesopor. Mater.* **2011**, *142*, 32–36.

(4) Položij, M.; Thang, H. V.; Rubeš, M.; Eliášová, P.; Čejka, J.; Nachtigall, P. Theoretical Investigation of Layered Zeolites with MWW Topology: MCM-22P vs. MCM-56. *Dalton Trans.* **2014**, *43*, 10443–10450.

(5) Ostroumova, V. A.; Maksimov, A. L. MWW-Type Zeolites: MCM-22, MCM-36, MCM-49, and MCM-56 (A Review). *Pet. Chem.* **2019**, *59*, 788–801.

(6) Roth, W. J.; Sasaki, T.; Wolski, K.; Ebina, Y.; Tang, D.-M.; Michiue, Y.; Sakai, N.; Ma, R.; Cretu, O.; Kikkawa, J.; Kimoto, K.; Kalahurska, K.; Gil, B.; Mazur, M.; Zapotoczny, S.; Čejka, J.; Grzybek, J.; Kowalczyk, A. Exfoliated Ferrierite-Related Unilamellar Nanosheets in Solution and Their Use for Preparation of Mixed Zeolite Hierarchical Structures. *J. Am. Chem. Soc.* **2021**, *143*, 11052–11062.

(7) Roth, W. J.; Gil, B.; Makowski, W.; Sławek, A.; Grzybek, J.; Kubu, M.; Čejka, J. Interconversion of the CDO Layered Precursor ZSM-55 between FER and CDO Frameworks by Controlled Deswelling and Reassembly. *Chem. Mater.* **2016**, *28*, 3616–3619.

(8) Metin, C. O.; Bonnecaze, R. T.; Lake, L. W.; Miranda, C. R.; Nguyen, Q. P. Aggregation Kinetics and Shear Rheology of Aqueous Silica Suspensions. *Appl. Nanosci.* **2014**, *4*, 169–178.

(9) Bayat, A. E.; Junin, R.; Ghadikolaei, F. D.; Piroozian, A. Transport and Aggregation of Al_2O_3 Nanoparticles through Saturated Limestone under High Ionic Strength Conditions: Measurements and Mechanisms. *J. Nanopart. Res.* **2014**, *16*, 2747.

(10) Baerlocher, C.; McCusker, L. B.; Brouwer, D.; Marler, B. *Database of Zeolite Structures*. https://www.iza-structure.org/databases/.